analytical chemistry

pubs.acs.org/ac Article

Assessing Local Electrical Properties of Ionic Liquid/Metal Interfaces with Operando-XPS and by Incorporating Additional Circuit Elements

Gozde Karaoglu, Ezgi Kutbay, Suleyman Ince, Burak Ulgut,* and Sefik Suzer*

Cite This: *Anal. Chem.* 2023, 95, 14861−14869 Read Online

ACCESS | Metrics & More | Article Recommendations | Supporting Information

ABSTRACT: X-ray photoelectron spectroscopy (XPS) has been utilized to record binding energy changes upon applying direct current (DC) and/or alternating current (AC) (square-wave) bias with different frequencies on a coplanar capacitor, having an ionic liquid (IL) film as the electrolyte. Electrical potential developments in numerous locations on the device are extracted from the variations in binding energy positions of the atomic core levels, which together with electrochemical measurements are used to extract local information before and after insertion of additional resistors in series. The presence of the IL introduces complex charging/discharging processes with a direct influence on the electrical double layer (EDL) formation, some of which can be untangled from each other via AC modulation by choosing appropriate time windows of observation. Accordingly, under 10 kHz modulation, fast processes are sampled, which are associated with electronic currents, and effects of slow migratory currents can be measured using 0.1 Hz. The addition of serial resistors allows us to quantify AC currents passing through, which reveals the magnitude of the system's impedance under different conditions. This process surprisingly reverses differences(s) in the voltage developments between the low and high frequencies over the electrified electrodes compared to those over the porous membrane in between. Our approach turns XPS into a powerful electrical and surface-sensitive tool for extracting localized electrochemical properties in a noninvasive and direct way. We expect that a wider utilization of the technique will lead to better identification of the obstacles for developing the next-generation sensing, energy harvesting, and storage systems as well as devices for iontronic/neuromorphic applications.

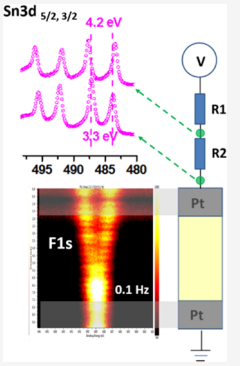

INTRODUCTION

Ionic liquids are composed of large organic/inorganic cations and anions that exhibit liquid-like properties at room temperature, and also have adequate electrical conductivity, usable for numerous electrochemical applications, including but not limited to being incorporated into devices as electrolytes.[1,2] This and other unique physical and chemical properties of ILs such as low volatility, high conductivity, larger operating potential window, and low toxicity[3−5] have led them to assume pivotal role(s) in fields such as biosystems, batteries, fuel cells, solar cells, supercapacitors, etc.[6−12]

Ionic motion across electrified electrodes, having liquid electrolytes in between, is the most important process controlling the performance of many electrochemical systems, spanning a wide range of micro- and macro-dimensions. The most important phenomenon affecting the ionic motion or transport in all of these systems has long been advocated to be the formation of the electrical double-layer (EDL) for both Faradaic and non-Faradaic processes since ions at the interface of the polarized/charged surfaces can and do rearrange to screen the charge on the electrode.[13] The resulting concentration and, therefore, the electrical potential profile at the electrode/electrolyte interface further triggers a multitude of processes controlling kinetics and thermodynamics of the electrochemical systems.[14] Therefore, investigations of static and dynamic properties of EDL formation have been in focus both experimentally and theoretically, dating back to Helmholtz for 17 decades.[15]

Recent progress on the investigation of the EDL formation process in systems and devices having ionic liquids include electrochemical,[16−20] microscopic,[21−23] terahertz imaging,[24] X-ray scattering techniques,[25,26] and electrochemical force microscopy,[27,28] all of which have been heavily guided and/or corroborated by modeling/simulation studies.[29,30] They all have contributed different and intriguing input into the dynamics of charge screening at the solid−liquid interfaces by identifying multiple time constants and relatively larger length scales of up to 10 μm.[27] On the other hand, using confocal fluorescence spectroscopic techniques, Blanchard et al. have reported on the detection of induced charge density gradients at even longer lateral (∼100 μm) distances.[31−33] But again, such distances are still small to represent real-life electrochemical devices. Moreover, information not only at the

Received: April 14, 2023
Accepted: September 14, 2023
Published: September 28, 2023

interfaces but also in regions covering the entire device is needed. Such measurements have also been reported by our group, utilizing a specific feature of X-ray photoelectron spectroscopy (XPS).[34]

XPS is a common chemical analysis tool used for extracting quantitative information with high surface sensitivity but with limited spatial resolution, on orders of 50−100 μm for most of the lab-based instruments. On the other hand, an underutilized advantage of XPS is its capability to faithfully reflect the local electrical potential profiles, vital for further advancement in applications of electrochemical systems. Core-level photoelectrons measured by XPS undergo binding energy shifts that reflect the local potential (V) on investigated surfaces in a chemically specific fashion, under an electrical bias, and the technique is also relatively noninvasive. Here, the binding energy uncertainty of the common lab-based instruments is about 20 meV. The expected low currents related to the photoelectron emission process are on the order of ∼1 nA, which translates to a negligibly small binding energy shift of ∼1 meV (IR drop) for a typical ionic liquid film device having ∼1 M·Ω overall resistance, which is way below the experimental error.

In one of the first XPS studies of ionic liquids, a drop of ionic liquid was placed on an inclined electrode.[35] That experimental setup enabled the formation of a liquid film thin enough to probe the IL/electrode interface such that the authors were able to follow the EDL processes by tracing the shifts in the core-level binding energies under bias. While the application of direct current (DC) bias during XPS data acquisition provides steady-state information, demonstrated by us[34] and others as well,[35−40] our group has previously shown that alternating current (AC) excitation is indispensable for investigation of the dynamics of electrical potential developments.[41−46] Use of scanning electron microscopy (SEM) for detecting similar changes due to potential induced intensity modulations was also recently reported by us.[47] Both our XPS and SEM investigations revealed that the effects of time-resolved polarization of the metal electrodes can be followed locally up to extremely long-distance (centimeters) and long-time (hundreds of seconds) ranges, in a chemically specific fashion.

Very recently, Yin et al. have reported on an investigation of a small (1 μm) and IL (DEME-TFSI)-based planar (two-electrode) capacitor, by recording (in vacuum) its transient current response to a fast-rising, and 0.1−4.0 V pulses, lasting a short duration (100 ms), for capturing a wide time-scale dynamics of the device, and commenting on its fast (micro-to-milliseconds) as well as a very long (10^{+5} s) time dependences.[48] Their findings on the extreme long time-scale dynamics are consistent with other previous reports using various physical measurements.[49−57]

Researchers working on the use of ILs as electrical double-layer transistors have also utilized different electrical/electrochemical techniques to tap into the dynamics of ion movements and/or ion transport within such devices in order to understand the intrinsic nature of the EDL charging and possibly establish simple procedures for distinguishing and quantification of electrostatic and electrochemical components.[58−62] One notable simple recipe advocated by Yuan et al. was to use very slow modulations, 0.1 Hz or below, as a practical cutoff for separating out the electrochemical contributions.[59]

As mentioned above, having reported on both the very-large lateral and very-long temporal behavior of the same IL (DEME-TFSI), we now extend our investigation using XPS and electrochemical measurements to capture certain features of the diffuse charge dynamics of a device in the form of a coplanar-plate capacitor geometry, having an IL as the electrolyte, while imposing a square-wave (AC) potential excitation with frequencies ranging from mHz to kHz at room temperature. Note that, for the commonly used parallel plate capacitor, the probing XPS beam would not have direct access to the electrode−electrolyte interface. Using a coplanar capacitor configuration instead, we are able to spatially extend the beam and probe the effects of screening of the applied potential through ionic movement across a large electrolyte medium since the ionic motion materializes in all regions of the device.

Square-wave, rather than conventional electrochemical sine-wave modulation, is preferred, since it causes almost no distortion of the XPS peaks. Moreover, we also incorporate additional and well-defined circuit (RC) elements in series with our IL-based coplanar capacitor to extract other electrical information and investigate this hybrid (electron−ion-conducting/iontronic) device using electrochemical, as well as XPS measurements, all in an ultrahigh-vacuum (UHV) environment. For recording XPS data on IL film, the F 1s peaks are used, but around the RC elements, we use Sn 3d spin−orbit peaks of the soldering joints to follow the potential developments upon imposing the external (DC and/or AC) stimuli.

With AC modulation, the changes in the voltage developments are captured within different time windows; hence, XPS functions as a local chemical oscilloscope, i.e., by dissecting the device and analyzing it point by point. The voltage information derived is unique and cannot be obtained by other electrical/electrochemical measurements. Still, it is somewhat different, since square-wave excitations are used to capture such information rather than the typical sine-waves used in classical electrochemical studies. But again, all natural/biosystems also use signals similar to ours.

Overall our work provides a simple yet invaluable experimental platform to be incorporated into numerous techniques for extracting novel and complementary information related to the dynamics of EDL formation for those working on various electrochemical devices and systems. Therefore, we expect that it will impact favorably on developments in EDL transistors, energy harvesting systems, and biomedical and neuromorphic applications.[60−63]

EXPERIMENTAL SECTION

The coplanar capacitor device configuration used in this study consists of two Pt electrodes deposited onto a porous polyethylene membrane (PEM, from Gelon LIB), which are used as the source and the drain electrodes, and a 5 μL ionic liquid (DEME-TFSI) is soaked to the uncovered membrane between them, acting as a continuous liquid film electrolyte medium. One of the electrodes is used as the working electrode for external biasing, and the other one, the counter electrode, is always kept at ground potential. A Thermo Fisher Kα XP spectrometer is used to record the F 1s, C 1s, and Sn $3d_{5/2}$ core-level spectra using 50 eV analyzer pass energy, but for time-resolved XPS measurements, the snapshot mode with 150 eV pass energy for fast data gathering is used instead of the scanning mode. Details of the experimental parameters and the

https://doi.org/10.1021/acs.analchem.3c01614
Anal. Chem. 2023, 95, 14861−14869

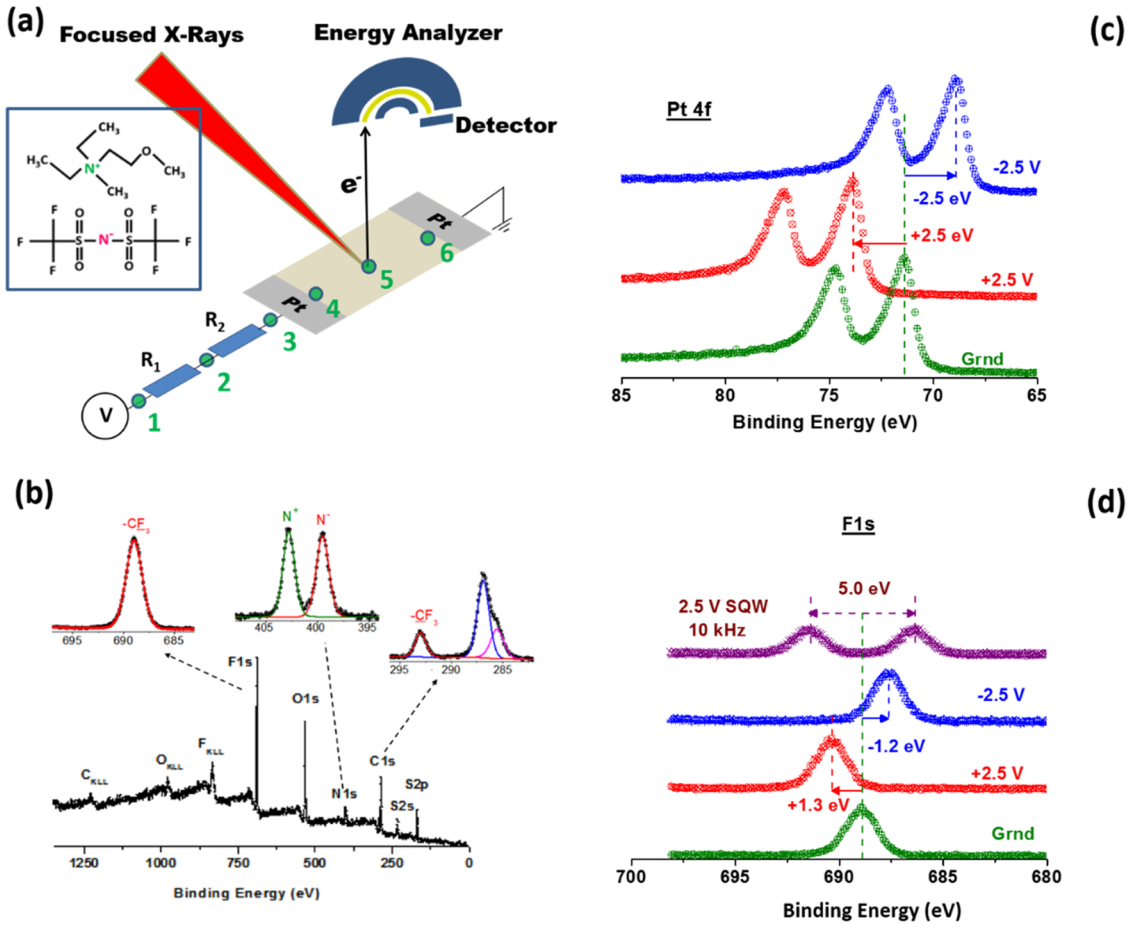

Figure 1. (a) Schematics of the coplanar capacitor, containing optional and additional resistors (R_1 and R_2), for probing dynamics of charging of the ionic liquid as the electrolyte, by the XPS probe beam, under operando conditions, where both current and peak positions are recorded simultaneously at different locations (green dots), also indicated as 1, 2, 3, 4, 5, and 6. The function generator is connected to the source electrode to impose a DC, or an AC (SQW) excitation with a fixed or variable frequency. The inset shows the chemical formula of the IL. (b) Survey and region's XP spectra of the IL. (c) Pt 4f XP Spectra, recorded at the source electrode and under 0, +2.5, and −2.5 V DC bias, and without the additional resistors. (d) F 1s XP spectra, recorded near the source electrode (position **4**), under 0, + 2.5, and −2.5 V DC bias, as well as under 2.5 V SQW excitation at 10 kHz.

devices used to implement the DC/AC biasing are given in the Supporting Information (SI).

Figure 1(a) displays a schematic representation of the device with the ionic liquid film and the platinum electrodes, which also shows two additional series resistors inserted. The chemical formula of the IL is displayed in the inset of Figure 1(a). XP survey spectrum of the IL, together with the scanned spectrum of the relevant atomic peaks, is depicted in Figure 1(b). Figure 1(c) shows the XP spectrum of the Pt 4f spin−orbit doublet, recorded on bare metal electrode and under −2.5, 0, and +2.5 V DC bias, respectively. Figure 1(d) shows the F 1s peak of the IL, recorded on the biased electrode (position **4**), and under the same biases, together with the same region recorded under 10 kHz, 2.5 V square-wave modulation.

XPS measures the kinetic energy and the intensity of the photoelectrons emitted under X-ray irradiation, which are also influenced by the local electrical potentials. A positive local potential impedes the kinetic energy, and a negative one enhances it, which appear as shifts in the binding energy positions recorded. As shown in Figure 1(c), the normal binding energy of the Pt $4f_{7/2}$ peak of metallic platinum appears at 71.2 eV but gets shifted to 73.7 and 68.7 eV under +2.5 and −2.5 V DC bias, respectively, thus faithfully complying with the DC bias. As depicted in Figure 1(d), the situation is quite different for the F 1s peak of the IL, which gets shifted only +1.3 and −1.2 eV, respectively, under the same DC biasing conditions. This is attributed to the screening of the applied potential by the formation of two electrical double layers (EDLs) at the two interfaces between the IL and the metallic source and drain electrodes.[34] The bias of 2.5 V was chosen to keep the Faradaic processes at a minimum yet provide reliable measurements of the peak position shifts.

Application of an SQW-AC bias twins each peak since both positive and negative cycles are imposed simultaneously. A schematic is included in Supporting Information Figure S1, where F 1s XP spectrum of the ionic liquid is used to elucidate the bias voltage shifts at the positive and negative cycles of the square-wave excitation, as well as the twinning of the peak as a result of the integration of all of them, within the 5 s data gathering time.

XP spectra of the F 1s region recorded under square- and sine-wave excitations are given in Figure S2 in the Supporting Information. Pertinent information is derived from both the positions of the twinned peaks and also the differences between them. Such is the case under 10 kHz bias, shown in

https://doi.org/10.1021/acs.analchem.3c01614
Anal. Chem. 2023, 95, 14861−14869

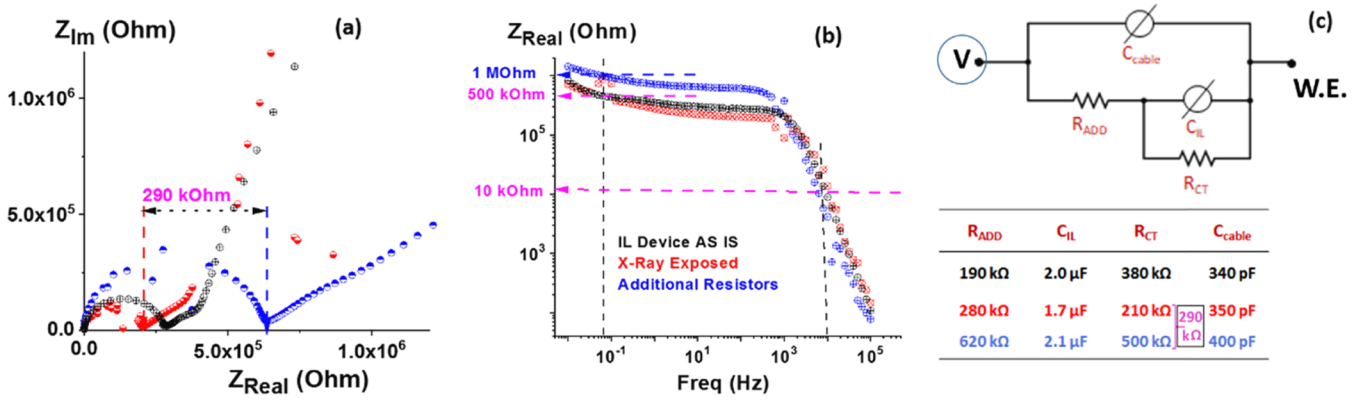

Figure 2. EIS measurements using the conventional sine-wave modulation at different frequencies for three different device configurations; (i) IL device AS IS (black), (ii) after exposure to X-rays for more than 8 h (red), and (iii) after introducing the additional resistors (blue). (a) Real and imaginary impedance values (Nyquist plots), where the additional resistors were quantified as 290 kΩ (see the text). (b) Impedance values of the overall system for the three different configurations under varying frequencies. A value of 10 kΩ is obtained at 10 kHz, as opposed to that of 1.0 MΩ at 0.1 Hz. (c) The model and the extracted electrical parameters for the three different device configurations.

Figure 1(d), which will be elaborated more below. Moreover, such variations differ significantly at different points along the device and also with the frequency of AC excitation. Accordingly, as we will show below, time-dependent voltage variations are captured, not only at different locations on the IL medium between the two electrodes but also at different locations on the metal electrode surfaces, which are also covered with IL.

Electrochemical impedance spectroscopy (EIS) data of the device with the ionic liquid at different stages are obtained by using a Gamry Reference 3000 instrument in potentiostatic mode. DC voltage is set to be 125 mV where the AC voltage is applied with an amplitude of 50 mV between 100 kHz and 10 mHz with 10 frequencies per decade. The connections are made through the sample holder and an external BNC cable to the instrument.

RESULTS AND DISCUSSION

Current−Voltage Measurements. In Figure S3(a) in the Supporting Information (SI), we summarize the current−voltage behavior of our device, by carrying out a series of cyclic voltammetric measurements, covering the range of ±0.125 to ±3.0 V under linear voltage ramps that are always completed in 200 s. Therefore, an increase in the voltage range also corresponds to an increase in the sweep rate as well. In Figure S3(b), the same graph is displayed after normalizing the measured currents, by dividing with the corresponding applied voltage for a better comparison, similar to those reported by Yin et al.[48] As can be gathered from the graphs, the electrochemical behavior of our system has a resemblance of a supercapacitor and also indicates the presence of other accompanying electrochemical processes, even as small as a voltage span from −0.125 to +0.125 V. Moreover and as has been already reported by us and others, upon application of even a small voltage bias, the induced current never dies away for time scales ∼10^4 s, as shown in Figure S4. In the cyclic voltammetry experiments, the currents that are scaled by sweep rate clearly increase as the voltage window is expanded, which is an indication of the existence of Faradaic processes.

Electrochemical Impedance Measurements. The EIS measurements were also carried out on the same device while it was inside the XPS UHV environment with and without additional resistors, which are depicted in Figure 2 along with the circuit model that was used to fit the data with the results, color-coded to indicate the correspondence.

In the model, the resistance that is in parallel to the capacitor (C_{IL}) represents the charge transfer (a.k.a Faradaic current) and C_{IL} represents the double-layer capacitance. R_{add} is the added resistor to the sample in addition to the existing resistance due to various inherent ones, and finally, C_{cable} is the capacitance that is due to the connectors and the BNC cable connecting the sample to the measuring instrument. Using our measurements, we determine this modeled R_{add} resistance to be ∼290 kΩ for the IL device, which is very close to the nominal (2 × 150 =) 300 kΩ value corresponding to the sum of the two resistors introduced, as also indicated in Figure 2(a).

Experimentally, the DC currents observed at longer times significantly decrease with the addition of a capacitor in series, as shown in Figure S5 in the SI. This is an indication that the Faradaic processes at a constant potential are somehow blocked by the existence of the additional capacitor. The added capacitor is favorable for DC studies, but it severely complicates the AC analysis; therefore, the AC analysis on this configuration is not presented here.

Overall, the addition of resistors in series significantly improves our ability to analyze the device. The comparisons that the added resistors allow are not directly available from measurements without them. This measurement is akin to the main idea behind using the Wheatstone Bridge, which allows for measuring the unknown via comparison with known circuit elements. These comparisons can also be carried out via the frequency dependence of voltage and current in order to identify and understand the details of the system. Given the complexity of the ionic liquids and the multitude of electronic/ionic phenomena that they exhibit, these comparisons provide invaluable information that cannot be obtained by isolated measurements.

In the model employed to fit the impedance spectrum, the much larger capacitance that is on the order of μF represents the double-layer capacitance of the ionic liquid and the capacitor in the range of 300 pF, which could be interpreted as the geometric capacitance or the cable capacitance.[64] The added resistor clearly shows up in parallel to the capacitor that is smaller, as evidenced by the fact that the diameter of the high-frequency semicircle increases by exactly the resistance amount of the added resistor (see Figure 2(a,c)). This is a clear

https://doi.org/10.1021/acs.analchem.3c01614
Anal. Chem. 2023, 95, 14861−14869

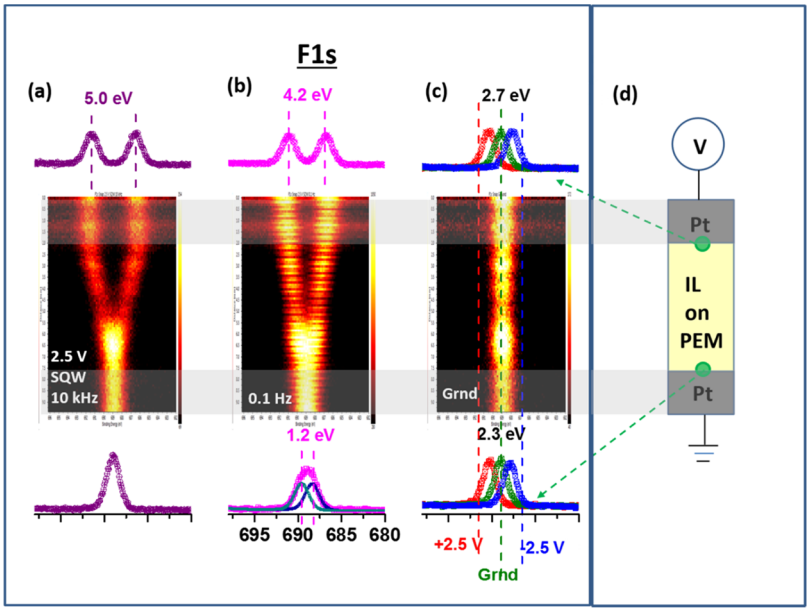

Figure 3. F 1s XP spectra recorded at different points on the device and under DC and AC-biasing conditions. (a) F 1s region's spectrum, recorded under 2.5 V SQW excitation and at 10 kHz frequency, near the biased electrode and near the grounded one, are shown at the top and the bottom traces, respectively. In the middle region, the 94 F 1s snapshot spectra are shown, recorded along the line starting from the top of the biased electrode, going all the way down to the end of the grounded electrode. (b) Same data collected under 0.1 Hz and (c) recorded under +2.5, 0, and −2.5 V DC excitations. (d) Schematics of the device.

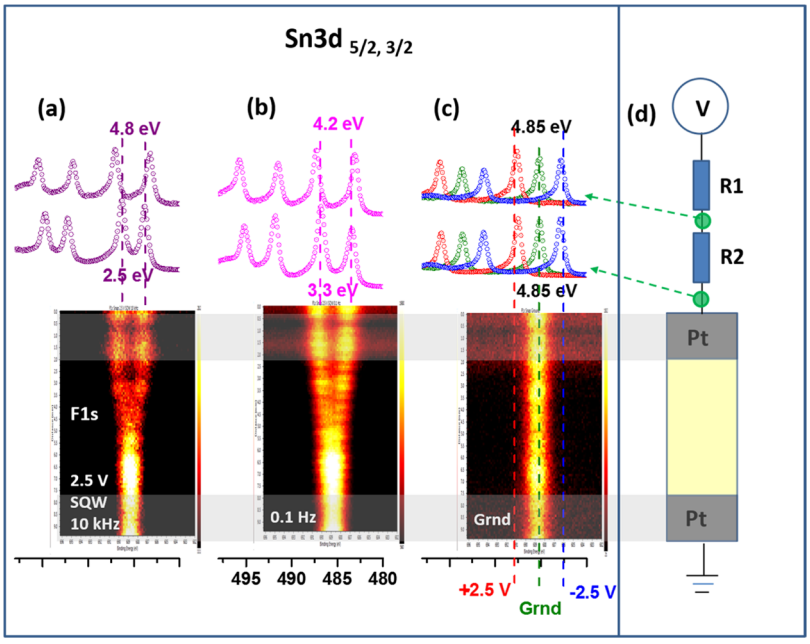

Figure 4. XPS Sn 3d and F 1s XP spectra recorded at different points on the device and under DC- and AC-biasing conditions after incorporating two resistors in series. (a) The upper part shows the Sn 3d spin−orbit doublet recorded after the 1st and 2nd resistors, and the lower part shows the 94 F 1s snapshot spectra recorded along the line starting from the top of the biased electrode, going all the way down to the end of the grounded electrode. (b) The same data collected under 0.1 Hz and (c) recorded under +2.5, 0, and −2.5 V DC excitations. (d) Schematics. The binding energy scale indicated in (b) refers to those of the Sn 3d peaks and not to the F 1s peak.

indication that the capacitance that is on the order of 300 pF is not due to the geometric effect of the two gold electrodes, but is due to a combination of cabling and sample holder capacitances.

In the same figure, the measured (or extracted) impedance values as a function of frequency are plotted in Figure 2(b), where more or less a plateau is observed in the low-frequency range up to about the kHz region, followed by a sharp decrease afterward. One can also see that although a clear distinction is observable by the additional resistors at low frequencies, this distinction is lost at the high-frequency range. These findings will give us invaluable guidance when we discuss the XPS results in the next section.

Operando-XPS Measurements. *IL Coplanar Device.* We used XPS to capture the local voltage variations at designated points along the device by recording the corresponding atomic

https://doi.org/10.1021/acs.analchem.3c01614
Anal. Chem. 2023, 95, 14861−14869

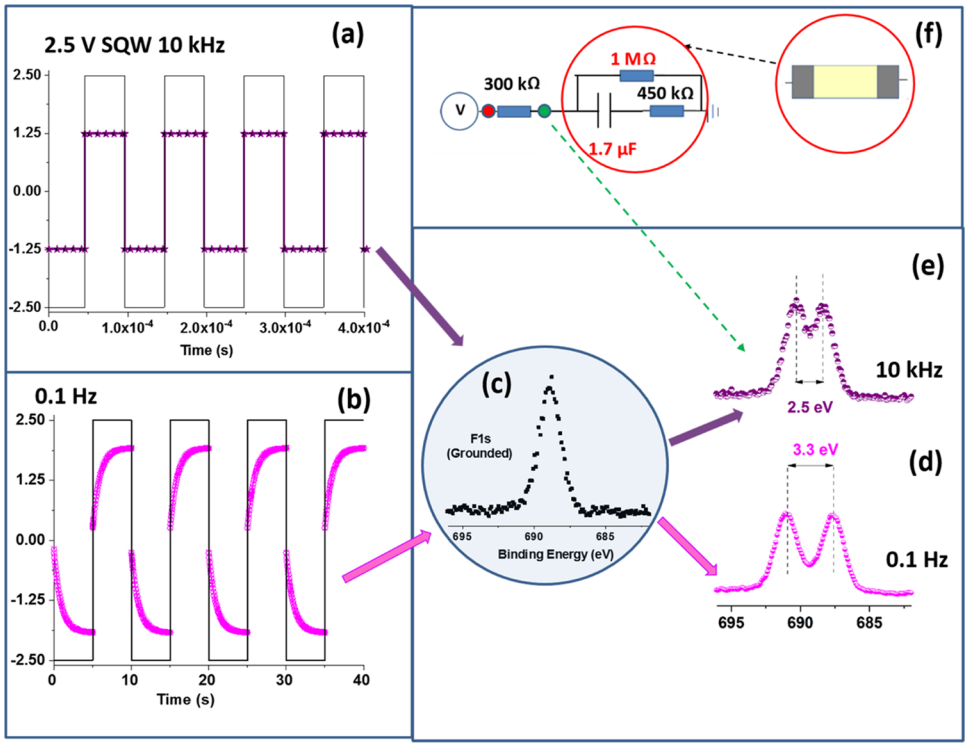

Figure 5. Simulation of the F 1s XP spectra recorded at the local point after the 2nd resistor and on the onset of the electrified Pt electrode, covered with the thin IL film. LT-spice voltage input and output under 2.5 V SQW modulations: at (a) 10 kHz and (b) 0.1 Hz. (c) XP spectrum of the F 1s under no-bias, used for the convolution process to yield the synthetic spectra under (d) 0.1 Hz and (e) 10 kHz. (f) Schematics of the setup and the equivalent circuit used.

core levels and extracting the shifts in the binding energy positions of the representative peaks under both DC and AC biasing. We also recorded those peaks along a designated line across the device. Since typically 70−100 points are involved in such a line-scan measurement, the faster, snapshot data recording route of the spectrometer is then used. In Figure 3, we depict a selection of such measurements of a relatively pristine IL device after a long outgassing and heating in vacuum procedure. Figure 3(a) gives the F 1s region's spectrum recorded under 2.5 V SQW excitation and at 10 kHz frequency near the biased electrode [position **4** of Figure 1(a)] and near the grounded one (position **5**), which are placed at the top and bottom traces, respectively. In the middle region, 94 F 1s snapshot spectra are shown along the line starting from the top of the biased electrode, going all the way down to the end of the grounded one. Figure 3(b) shows the same data collected at 0.1 Hz. In Figure 3(c), the F 1s region, recorded under +2.5, 0, and −2.5 V DC measurements near electrode and near ground, is displayed at the top and bottom of the figure, respectively, while only the grounded line-scan spectra are shown in the middle trace.

Selection of the two AC frequencies is not arbitrary but reflects the time windows corresponding to the predominantly electronic polarization of the bulk ionic liquid at 10 kHz, and to the migratory motion dominated by ions at 0.1 Hz, as discussed in our earlier work,[48,65] and as was also advocated by Frisbie et al.[61] The idea behind lies in the possibility of separating the contributions of the above-mentioned two motions (i.e., bulk polarization vs electrochemical). Accordingly, measurements at 10 kHz (i.e., within 0.1 μs time window) reflect the potential variations of the initial electric field imposed by the bias. This is translated to V-shaped binding energy shifts between the two electrodes since the twinned peaks appear at ±2.5 eV shifted positions, i.e., with 5.0 eV separation on the electrified electrode. This difference decreases linearly along the IL film, disappearing completely at the grounded electrode. Such a V-shaped spectral feature points to zero effective screening measured at 10 kHz along the ionic liquid film.

This situation differs at 0.1 Hz (5 s time window), and significant screening is revealed not only between the electrodes but also all over the device, including both electrode regions. Finally, under the DC actuation (>10^3 s time window), the equilibrium screened position is approached, which in the ideal case should be 1/2 of the applied bias (1.25 eV).[34]

IL Coplanar Device with 2 Series Resistors. Having learned some of the electrical properties using the EIS as well as biased-XPS results, as the second step, we have included two equivalent 150 kΩ resistor elements in series with the device described above and inserted all of them into the UHV chamber of the XPS instrument and carried out similar XPS measurements. The resulting spectra are summarized in Figure 4, yielding a wealth of pertinent information. Note in passing, when we introduced the series resistors from outside of the spectrometer via the power supply's BNC connector, reliable XP spectra could not be recorded under AC modulation conditions, as shown in Figure S6 in the Supporting Information.

The complementing information about the changes in the local potential variations within the IL device due to the resistors added is harmonious and continuous, under both high and low frequencies, which are revealed via the recorded Sn 3d and F 1s XP spectra displayed in Figure 4. The voltage drops at

https://doi.org/10.1021/acs.analchem.3c01614
Anal. Chem. 2023, 95, 14861−14869

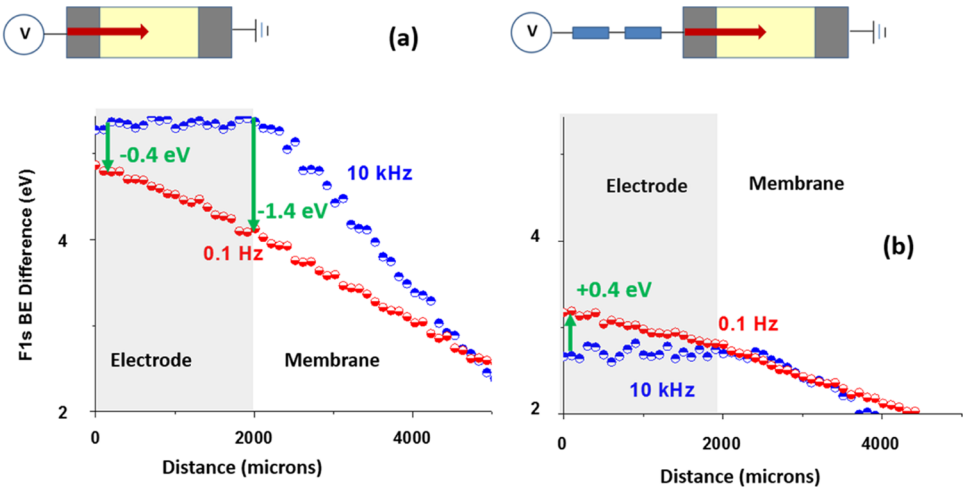

Figure 6. Measured binding differences between the twinned peaks under 10 kHz and 0.1 Hz SQW modulations and along the red arrow designated over and around the electrified electrode. (a) Device with only the IL. (b) Together with the added resistors.

different positions across the entire device can now be quantified using the binding energy positions and/or differences recorded under 3 distinct 2.5 V electrical biasing conditions; (i) the fast 10 kHz, (ii) the slow 0.1 Hz SQW modulations, and (iii) DC.

Under AC bias, deviations in the binding energy difference, recorded from the applied 5.0 V gives directly the local potential values. Accordingly, under 10 kHz, the measured B.E. difference between the twinned Sn $3d_{5/2}$ peaks is 3.8 eV at the point after R1 and decreases to 2.5 eV after R2. Hence, the corresponding two voltage drops are (5.0−3.8 =) 1.2 V and (3.8−2.5 =) 1.3 V, respectively. These voltage drops across the additional elements are equal to each other within our experimental uncertainty, as expected since the resistor values are equivalent. This finding also points out that the remaining 2.5 V drop occurs through the IL device. One can now calculate the AC current as 2.5 V = 300 kΩ × I_{Dev}, to yield ∼8.3 μA, and approximately 300 kΩ impedance (AC resistance) against the 10 kHz SQW modulation for the IL device. This value differs at least 1 order of magnitude from that obtained using the EIS measurements of Figure 3(a), which can probably be attributed to the different response of the system to the 2.5 V square waves we employ in XPS, compared to the very low-amplitude sine waves that are used in recording the EIS data.

A similar analysis can also be done for the 2.5 V SQW with 0.1 Hz data, using the data presented in Figure 4(b), where smaller deviations from the full 5 V peak-to-peak are obvious due to the voltage drop across the series resistors. The F 1s B.E. difference measured at the electrified electrode is now 3.3 eV, revealing that the voltage drop across the two resistors is 1.7 eV smaller than 2.5 eV measured at 10 kHz, signaling that effective AC resistance has increased to ((3.3/1.7) × 300 kΩ =) ∼580 kΩ, which again differs from the EIS measurements, and might again be attributed to the very large amplitude of 2.5 V SQW applied and different modes of excitations. The question then arises about the possibility of using a simple electrical circuit modeling for the variable nature of the impedance such that it will lead to spectral features consistent with the XPS results.

Equivalent Circuit Modeling. As we have already reported in our previous work on the use of XPS for probing electrowetting properties of ionic or other liquid drops on dielectrics (EWOD), we could utilize the commonly consulted LT-Spice simulation program to compare its output with those obtained from XPS measurements.[65,66] Basically, the voltage output provided by the program, at different local positions along the device and at the designated frequencies, was convoluted with the IL's F 1s region's XP spectrum recorded under no bias, to mimic the spectra obtained under AC modulations as depicted in Figure 5, and also in Figure S8 in the SI. In order to match the XPS data, we have to introduce an additional parallel resistor of ∼1 MΩ value, which also matches with the limiting (>300 s) value obtained under 2.5 V pulsed excitation (see Figures S4 and S5). Moreover, the serial resistance of the IL device has to be changed to a value of 450 kOhm so that we get back the impedance values measured by XPS with and without the additional 300 kΩ resistor. As a result, the synthetic spectra obtained by convolution of the F 1s spectrum under no-bias with the simulated voltage values obtained from the LT-Spice program using the circuit elements designated in Figure 5(f) faithfully reproduce the XP spectra recorded under both 10 kHz and 0.1 Hz. Measured binding energy positions of the relevant elements and their differences are given in Table S1 in the SI, at different local points of the device and under various biasing conditions.

For ensuring the reliability of our measurements under bias, XP spectra are also recorded on the gold arm, which connects the device inside the vacuum system to the external power supplies, i.e., at the point **1** designated in Figure 1(a). The corresponding Au 4f XP spectra are given in Figure S7 in the SI. The Au 4f doublets are faithfully twinned with an exact separation of 5.0 eV under 2.5 V SQW excitation at all frequencies [Figure S6(a)]. The situation is drastically different after connecting the systems through an externally introduced series resistance, and the shifts deviate more as the frequency of the excitation is increased [Figure S6(b)], validating our methodology's soundness.

Local Voltage Variations on the Electrified Electrode. Having learned that the voltage developments are different under high (10 kHz) and low (0.1 Hz) frequencies and also at different locations, we now turn to their manifestations over the electrodes' area. To do that, we take the binding energy difference between the twinned F 1s peaks and identify them as the reflectors of the changes in the potential developments within the designated time window (i.e., 5 s to 50 ms = ∼5 s).

https://doi.org/10.1021/acs.analchem.3c01614
Anal. Chem. 2023, 95, 14861−14869

These changes are plotted as a function of position over the electrified electrode in Figure 6. The surprising finding is that the changes display opposite behavior over the electrified electrode after adding the resistors.

One factor that might contribute to the observed sign reversal is the change in the magnitude of the electrical fields under high and low AC frequencies, on account of the increase in the impedance of the system at low frequencies since the resistance values of the added additional elements do not change with frequency. However, this hypothesis was checked out by another measurement performed on a similar device (not shown) at a higher AC amplitude of 4 V SQW, again at 10 kHz and 0.1 Hz, where we observed that the same opposite behavior and even larger differences persist. Therefore, other factors must be considered, such as the ionic motion/flow in two dimensions within the liquid layer, i.e., along the direction of the electrodes, as well as over and above them.

On the other hand, the fact that we can detect and quantify voltage developments locally due to ionic screening calls for designing and testing a myriad of different geometrical and/or chemical variations for identifying the key parameters toward better understanding of the ionic motion and the EDL formation. Needless to say that theoretical modeling and/or simulations would contribute significantly to these issues of paramount importance.

CONCLUSIONS

We have amalgamated current−voltage and EIS measurements with localized XPS ones under DC and square-wave (AC) modulation, to extract additional information about the charging dynamics of a coplanar capacitor in macro-dimensions, having an ionic liquid film as the electrolyte medium. Shifts in the measured binding energy positions of the relevant XPS core levels were used to infer the local electrical potential developments under bias, and the incorporation of external circuit elements was extremely useful for quantifying the AC impedance of the device, which were found to be dependent on the frequency applied. Accordingly, it turned out that the voltage variations are substantially different over the electrodes after the addition of solid-state resistors. The addition of a resistor effectively improves the resolution of the measurements much like the bridge-type comparative measurements and thus enables the amplification of the inherent properties in the electrical results. Therefore, we are hoping that using local XPS data extracted from the high (10 kHz) and low (0.1 Hz) frequencies, the chemical/physical nature of the contributing processes to the localized voltage developments could be faithfully identified and quantified. The ultimate goal is, of course, to use the approach for assessing the individual contribution(s) and the effect(s) of the chemical/physical nature of the constituents (i.e., anions and cations, and electrodes) to the electrical potential developments. Presently, we are carrying out work along these directions and hope that other researchers will follow us. The methodology is simple to implement, and the extracted data are unique, which can be utilized to interrogate especially the mixed or hybrid electronic/ionic conducting systems for advanced applications in sensing, energy harvesting, and storage devices, as well as in neuromorphic materials applications.

ASSOCIATED CONTENT

Supporting Information

The Supporting Information is available free of charge at https://pubs.acs.org/doi/10.1021/acs.analchem.3c01614.

Schematics of the data gathering procedure under AC modulation and under square and sine waves; additional data about the chemicals and instruments used; *I*−*V* measurements under various conditions and XP spectra recorded under AC modulation when the resistors were introduced from outside and inside of the UHV system; spectra for validating our measurements, as well as details of the simulations for using LT-spice output convoluted with the grounded F 1s spectrum; a table containing the measured binding energy positions of the relevant elements, and their differences at different local points of the device and under various biasing conditions (PDF)

AUTHOR INFORMATION

Corresponding Authors

Burak Ulgut − *Department of Chemistry, Bilkent University, 06800 Ankara, Turkey;* orcid.org/0000-0002-4402-0033; Email: ulgut@fen.bilkent.edu.tr

Sefik Suzer − *Department of Chemistry, Bilkent University, 06800 Ankara, Turkey;* orcid.org/0000-0002-5866-2600; Email: suzer@fen.bilkent.edu.tr

Authors

Gozde Karaoglu − *Department of Chemistry, Bilkent University, 06800 Ankara, Turkey*

Ezgi Kutbay − *Department of Chemistry, Bilkent University, 06800 Ankara, Turkey*

Suleyman Ince − *Department of Chemistry, Bilkent University, 06800 Ankara, Turkey;* orcid.org/0000-0002-1203-6313

Complete contact information is available at: https://pubs.acs.org/10.1021/acs.analchem.3c01614

Notes

The authors declare no competing financial interest.

REFERENCES

(1) Liu, R.; Zhao, S.; Liu, J. *ACS Appl. Electron. Mater.* **2021**, *3* (1), 101−118.

(2) Zhu, C.; Huang, K.; Siepser, N. P.; Baker, L. A. *Chem. Rev.* **2021**, *121* (19), 11726−11768.

(3) Hansen, B. B.; Spittle, S.; Chen, B.; Poe, D.; Zhang, Y.; Klein, J. M.; Horton, A.; Adhikari, L.; Zelovich, T.; Doherty, B. W.; Gurkan, B.; Maginn, E. J.; Ragauskas, A.; Dadmun, M.; Zawodzinski, T. A.; Baker, G. A.; Tuckerman, M. E.; Savinell, R. F.; Sangoro, J. R. *Chem. Rev.* **2021**, *121* (3), 1232−1285.

(4) Egorova, K. S.; Gordeev, E. G.; Ananikov, V. P. *Chem. Rev.* **2017**, *117* (10), 7132−7189.

(5) Watanabe, M.; Thomas, M. L.; Zhang, S.; Ueno, K.; Yasuda, T.; Dokko, K. *Chem. Rev.* **2017**, *117* (10), 7190−7239.

(6) Welton, T. *Biophys. Rev.* **2018**, *10* (3), 691−706.

(7) Tian, Y.; Zeng, G.; Rutt, A.; Shi, T.; Kim, H.; Wang, J.; Sun, Y.; Ouyang, B.; Chen, T.; Lun, Z.; Rong, Z.; Persson, K.; Ceder, G. *Chem. Rev.* **2021**, *121* (3), 1623−1669.

(8) Chen, K.; Yang, D.-Y.; Huang, G.; Xhang; Zhang, X.-B. *Acc. Chem. Res.* **2021**, *2* (7), 632−641.

(9) Selvaraj, B.; Shanmugam, G.; Kamaraj, S.; Gunasekeran, A.; Sambandam, A. *Inorg. Chem.* **2021**, *60* (3), 1937−1947.

(10) Eftekhari, A. *Energy Storage Mater.* **2017**, *9*, 47−69.

(11) Simon, P.; Gogotsi, Y. *Nat. Mater.* **2020**, *19*, 1151−1163.
(12) Miao, L.; Song, Z.; Zhu, Z.; Li, L.; Gan, L.; Liu, M. *Energy Fuels* **2021**, *35* (10), 8443−8455.
(13) Bard, A. J.; Faulkner, L. R. *Electrochemical Methods: Fundamentals and Applications*; Wiley, 2000.
(14) Dickinson, E. J. F.; Compton, R. G. *J. Electroanal. Chem.* **2011**, *661* (1), 198−212.
(15) Grahame, D. C. *Chem. Rev.* **1947**, *41* (3), 441−501.
(16) Lockett, V.; Sedev, R.; Ralston, J.; Horne, M.; Rodopoulos, T. *J. Phys. Chem. C* **2008**, *112* (19), 7486−7495.
(17) Lockett, V.; Horne, M.; Sedev, R.; Rodopoulos, T.; Ralston, J. *Phys. Chem. Chem. Phys.* **2010**, *12* (39), 12499−12512.
(18) Druschler, M.; Huber, B.; Roling, B. *J. Phys. Chem. C* **2011**, *115*, 6802−6808.
(19) Zheng, J.; Moganty, S. S.; Goonetilleke, P. C.; Baltus, R. E.; Roy, D. *J. Phys. Chem. C* **2011**, *115* (15), 7527−7537.
(20) Jitvisate, M.; Seddon, J. R. T. *J. Phys. Chem. Lett.* **2018**, *9*, 126−131.
(21) Hayes, R.; Borisenko, N.; Tam, M. K.; Howlett, P. C.; Endres, F.; Atkin, R. *J. Phys. Chem. C* **2011**, *115* (14), 6855−6863.
(22) Atkin, R.; Borisenko, N.; Drüschler, M.; Endres, F.; Hayes, R.; Huber, B.; Roling, B. *J. Mol. Liq.* **2014**, *192*, 44−54.
(23) Hayes, R.; Warr, G. G.; Atkin, R. *Chem. Rev.* **2015**, *115* (13), 6357−6426.
(24) Baylam, I.; Cizmeciyan, M. N.; Balci, O.; Ozharar, S.; Kakenov, N.; Polat, E. O.; Kocabas, C.; Kocabas, C.; Sennaroglu, A. *Opt. Lett.* **2014**, *39* (2014), No. 5180.
(25) Uysal, A.; Zhou, H.; Feng, G.; Lee, S. S.; Li, S.; Cummings, P. T.; Fulvio, P. F.; Dai, S.; McDonough, J. K.; Gogotsi, Y.; Fenter, P. *J. Phys.: Condens. Matter.* **2015**, *27* (3), No. 032101.
(26) Chu, M.; Miller, M.; Douglas, T.; Dutta, P. *J. Phys. Chem. C* **2017**, *121* (7), 3841−3845.
(27) Collins, L.; Jesse, S.; Kilpatrick, J. I.; Tselev, A.; Varenyk, O.; Okatan, M. B.; Weber, S. A. L.; Kumar, A.; Balke, N.; Kalinin, S. V.; Rodriguez, B. J. *Nat. Commun.* **2014**, *5* (1), No. 3871.
(28) Collins, L.; Kilpatrick, J. I.; Kalinin, S. V.; Rodriguez, B. J. *Rep. Prog. Phys.* **2018**, *81* (8), No. 086101.
(29) Bedrov, D.; Piquemel, J.-P.; Borodin, O.; MacKerell, A. D.; Roux, B.; Schroder, C. *Chem. Rev.* **2019**, *119* (13), 7940−7995.
(30) Wang, Y.-L.; Li, B.; Sarman, S.; Mocci, F.; Lu, Z.-Y.; Yuan, J.; Laaksonen, A.; Fayer, M. D. *Chem. Rev.* **2020**, *120* (13), 5798−5877.
(31) Ma, K.; Jarosova, R.; Swain, G. M.; Blanchard, G. J. *Langmuir* **2016**, *32*, 9507−9512.
(32) Ma, K.; Jarosova, R.; Swain, G. M.; Blanchard, G. J. *J. Phys. Chem. C* **2018**, *122*, 7361−7367.
(33) Wang, Y.; Jarosova, R.; Swain, G. M.; Blanchard, G. J. *Langmuir* **2020**, *36*, 3038−3045.
(34) Camci, M. T.; Aydogan, P.; Ulgut, B.; Kocabas, C.; Suzer, S. *Phys. Chem. Chem. Phys.* **2016**, *18* (41), 28434−28440.
(35) Weingarth, D.; Foelske-Schmitz, A.; Wokaun, A.; Kötz, R. *Electrochem. Commun.* **2011**, *13* (6), 619−622.
(36) Greco, F.; Shin, S.; Williams, F. J.; Heller, B. S. J.; Maier, F.; Steinrück, H. P. *ChemistryOpen* **2019**, *8*, 1365−1368.
(37) Jia, M.; Broderick, A.; Newberg, J. T. *ChemPhysChem* **2021**, *22*, 633−640.
(38) Kruusma, J.; Tõnisoo, A.; Pärna, R.; Thomberg, T.; Kook, M.; Romann, T.; Kisand, V.; Lust, E. *J. Electroanal. Chem.* **2021**, *897*, 115561−115571.
(39) Shin, S.; Greco, F.; Maier, F.; Steinruck, H. P. *Phys. Chem. Chem. Phys.* **2021**, *23*, 10756−10762.
(40) Greco, F.; Hemmeter, D.; Shin, S.; Steinruck, H.-P.; Maier, F. *J. Ionic Liq.* **2022**, *2*, No. 100019.
(41) Gokturk, P. A.; Ulgut, B.; Suzer, S. *Langmuir* **2019**, *35* (9), 3319−3326.
(42) Uzundal, C. B.; Sahin, O.; Gokturk, P. A.; Wu, H.; Mugele, F.; Ulgut, B.; Suzer, S. *Langmuir* **2019**, *35* (52), 16989−16999.
(43) Gokturk, P. A.; Ulgut, B.; Suzer, S. *Langmuir* **2018**, *34* (25), 7301−7308.
(44) Uzundal, C. B.; Gokturk, P. A.; Suzer, S.; Ulgut, B. *J. Phys. Chem. C* **2019**, *123* (21), 13192−13200.
(45) Gokturk, P. A.; Camci, M. T.; Suzer, S. *J. Vac. Sci. Technol., A* **2020**, *38* (4), No. 040805.
(46) Gokturk, P. A.; Suzer, S. *J. Phys. Chem. C* **2021**, *125*, 9453−9460.
(47) Suzer, S.; Strelcov, E.; Kolmakov, A. *Anal. Chem.* **2021**, *93*, 13268−13273.
(48) Yin, S.; He, K.; Randle, M. D.; Barut, B.; Dixit, R.; Lipatov, A.; Sinitskii, A.; Bird, J. *J. Phys. Chem. C* **2022**, *126*, 1958−1965.
(49) Schmidt, E.; Shi, S.; Ruden, P. P.; Frisbie, C. D. *ACS Appl. Mater. Interfaces* **2016**, *8*, 14879−14884.
(50) Gebbie, M. A.; Valtiner, M.; Banquy, X.; Fox, E. T.; Henderson, W. A.; Israelachvili, J. N. *Proc. Natl. Acad. Sci. U.S.A.* **2013**, *110* (24), 9674−9679.
(51) Gebbie, M. A.; Smith, A. M.; Dobbs, H. A.; Lee, A. A.; Warr, G. G.; Banquy, X.; Valtiner, M.; Rutland, M. W.; Israelachvili, J. N.; Perkin, S.; Atkin, R. *Chem. Commun.* **2017**, *53* (7), 1214−1224.
(52) Lee, A. A.; Perez-Martinez, C. S.; Smith, A. M.; Perkin, S. *Faraday Discuss.* **2017**, *199* (0), 239−259.
(53) Fillaud, L.; Petenzi, T.; Pallu, J.; Piro, B.; Mattana, G.; Noel, V. *Langmuir* **2018**, *34*, 3686−3693.
(54) Perez-Martinez, C. S.; Perkin, S. *Soft Matter* **2019**, *15*, 4255−4265.
(55) Richter, L.; Zuk, P. J.; Paczensy, J.; Bak, K. M.; Szymborski, T.; Garstecki, P.; Stone, H. A.; Holyst, R.; Drummond, C. *Phys. Rev. Lett.* **2020**, *125*, No. 056001.
(56) Han, M.; Kim, H.; Leal, C.; Negrito, M.; Batteas, J. D.; Espinosa-Marzal, R. M. *Adv. Mater. Interfaces* **2020**, *7*, No. 2001313.
(57) Belotti, M.; Lyu, X.; Halat, P.; Darwish, N.; Silvester, D. S.; Goh, C.; Izgorodina, I.; Coote, M. L.; Ciampi, C. *J. Am. Chem. Soc.* **2021**, *143*, 17431−17440.
(58) Yuan, H.; Shimotani, H.; Tsukazaki, A.; Ohtomo, A.; Kawasaki, M.; Iwasa, Y. *Adv. Funct. Mater.* **2009**, *19*, 1046−1053.
(59) Yuan, H.; Shimotani, H.; Ye, J.; Yoon, S.; Aliah, H.; Tsukazaki, A.; Kawasaki, M.; Iwasa, Y. *J. Am. Chem. Soc.* **2010**, *132*, 1802−18407.
(60) Du, H.; Lin, X.; Xu, Z.; Chu, D. *J. Mater. Sci.* **2015**, *50*, 5641−5673.
(61) Schmidt, E.; Shi, S.; Ruden, P. P.; Frisbie, C. D. *ACS Appl. Mater. Interfaces* **2016**, *8*, 14879−14884.
(62) Huang, H.; Ge, C.; Liu, Z.; Zhong, H.; Guo, E.; He, M.; Wang, C.; Yang, G.; Jin, K. *J. Semicond.* **2021**, *42*, No. 013103.
(63) Abasi, S.; Aggas, J. R.; Garayar-Levya, G. G.; Wlather, B. K.; Guiseppi-Elie, A. *ACS Meas. Sci. Au* **2022**, *2*, 495−516, DOI: 10.1021/acsmeasuresciau.2c00033.
(64) Orazem, M. E.; Tribollet, B. *Electrochemical Impedance Spectroscopy*, 2nd ed.; John Wiley & Sons: Hoboken, NJ, 2017.
(65) Gokturk, P. A.; Ulgut, B.; Suzer, S. *Langmuir* **2019**, *35*, 3319−3326.
(66) Uzundal, C. B.; Sahin, O.; Gokturk, P. A.; Wu, H.; Mugele, F.; Ulgut, B.; Suzer, S. *Langmuir* **2019**, *35*, 16989−16999.

https://doi.org/10.1021/acs.analchem.3c01614
Anal. Chem. 2023, 95, 14861−14869